Monthly Notices of the ROYAL ASTRONOMICAL SOCIETY

MNRAS **527,** 2781–2789 (2024) https://doi.org/10.1093/mnras/stad3315
Advance Access publication 2023 October 28

Characterization of acetonitrile ice irradiated by X-rays employing the PROCODA code – II. Desorption processes

G. A. Carvalho [1,2]★ S. Pilling[3] and S. Gerasimenko[1]

[1] *Departamento de Física, Universidade Tecnológica Federal do Paraná, Medianeira 85884-000, PR, Brazil*
[2] *Programa de Pós-Graduação em Física e Astronomia, Universidade Tecnológica Federal do Paraná, Jardim das Americas, Curitiba 82590-300, PR, Brazil*
[3] *Instituto de Pesquisa e Desenvolvimento, Universidade do Vale do Paraíba, São José dos Campos 12244-000, SP, Brazil*

Accepted 2023 October 23. Received 2023 October 16; in original form 2023 August 14

ABSTRACT

In this work, we focus on the study of radiation-induced desorption processes that occurred in acetonitrile ice irradiated by broad-band X-rays (6 eV to 2 keV) monitored by Fourier transform infrared spectroscopy at different radiation fluences. In a previous work, we used the PROCODA code to derive the chemical evolution of the ice. Here, we have observed that the acetonitrile desorbed column density is at least two orders of magnitude larger than the desorbed column densities of daughter or granddaughter molecular species at chemical equilibrium stage. This indicates that total desorption column density is mainly governed by the father molecule, as also previously hypothesized in experimental studies. This occurs basically because the acetonitrile column density is larger than the other ones. In particular, at chemical equilibrium acetonitrile desorption column density represents almost 98 per cent of the total, while it is close to 1 per cent for H, CN, and CH_2, the species with larger molecular desorption percentages at chemical equilibrium. Another derived quantity is what we called intrinsic desorption rate, which is a number per second for individual species. Some of the larger intrinsic desorption rates were 6.2×10^{-6} (CH_3CN), 6.2×10^{-6} (CN), 5.7×10^{-6} (H), 5.7×10^{-6} (CH_2), and 4.4×10^{-6} (C_2N_2). These results help to put constraints in astrochemical models and can also be useful to clarify some astronomical radio observations.

Key words: astrochemistry – molecular processes – software: simulations – X-rays: stars.

1 INTRODUCTION

The radiation chemistry, important for the chemical evolution of molecular species in several astrophysical scenarios, involves a lot of phenomena, such as photodissociation, ionization, and desorption to gas phase of astrophysical ices (Moore, Khanna & Donn 1991; Moore, Ferrante & Nuth 1996; Kanda, Nagata & Ibuki 1999; Hudson & Moore 2006; Pilling et al. 2010; Vasconcelos et al. 2017). The last one determines molecular abundances at gas phase; e.g. the gas-phase abundance of acetonitrile in protoplanetary discs is not entirely explained by pure gas-phase reactions, so it is probably connected to the acetonitrile desorption on the surface of ice mantles (Öberg et al. 2015; Loomis et al. 2018; Basalgéte et al. 2021, 2023).

In fact, most molecular species are expected to be formed on the surface of the interstellar dust grains being later desorbed to gas phase. Therefore, the material in ice phase is a source for increasing molecular complexity of the gas phase in the interstellar medium. The *JWST* observations of interstellar ices in star-forming regions are revealing new details of ice evolution based on infrared (IR) features of frozen molecules. These observations in connection with laboratory investigations will give even further details on the acetonitrile gas-phase formation.

Acetonitrile is a precursor of more complex nitrile molecules in space environments (Gerakines, Moore & Hudson 2004). It has been detected in many different situations: in comets (Huebner, Snyder & Buhl 1974; Crovisier 1998; Woodney et al. 2002; Goesmann et al. 2015), protoplanetary discs (Öberg et al. 2015; Bergner et al. 2018), interstellar medium (Snyder & Buhl 1971; Solomon et al. 1971; Beltrán et al. 2006), molecular clouds (Willis et al. 2020), moons' atmosphere (Lara et al. 1996; Marten et al. 2002; Thelen et al. 2019, 2020; Iino, Sagawa & Tsukagoshi 2020), hot cores (Bøgelund et al. 2019), and high/low-mass protostars (Andron et al. 2018; Taniguchi et al. 2020). In addition, it is also among the five interstellar complex molecules desorbed by the frozen mantle of the circumstellar disc around the V883 Orionis protostar (Lee et al. 2019) and it is a commonly detected organic molecule in discs (Le Gal et al. 2019).

Using the Atacama Large Millimeter Array (ALMA) radio telescope, organic molecules were tracked in the protoplanetary discs of five stars: IM Wolf, AS 209, GM Aurigae, HD 163 296, and MWC 480 (Thelen et al. 2019; Iino, Sagawa & Tsukagoshi 2020; Willis et al. 2020; Öberg et al. 2021). The authors have been able to trace simple organic molecules, including HCN, C_2H, H_2CO, HC_3N, and also CH_3CN. The molecules have been found in the inner regions of the discs, where planets are likely to form. These molecules can, under the right conditions, serve as 'building blocks' for the substances of terrestrial biochemistry: sugars, amino acids, and even components of ribonucleic acid.

★ E-mail: gacarvalho@utfpr.edu.br

Recently, vacuum ultraviolet (VUV) with energy in the range 7–13.6 eV was used to derive the photodesorption yields of pure CH_3CN and CO and H_2O admixed acetonitrile (Basalgéte et al. 2021). Their results show that the photodesorption spectra of acetonitrile and its fragments (e.g. HCN, CN, CH_3) do not depend on the coadsorption of CH_3CN with CO and H_2O, which are dominant in astrophysical scenarios. More recently, the photodesorption of X-ray irradiated acetonitrile was also obtained (Basalgéte et al. 2023); their values help to understand the gas-phase abundances of acetonitrile in protoplanetary discs. The thermal desorption of acetonitrile was also discussed in Corazzi et al. (2021) and Carvalho & Pilling (2022), where results indicate that thermal desorption depends weakly on ice composition, and it peaks around 120–300 K.

In a previous work (hereafter paper I), we used the PROCODA code – a code developed to model the chemical evolution of the ice samples based on experimental data of irradiated astrophysical ice analogues – to study the X-ray irradiation of a pure acetonitrile ice sample (Carvalho, Pilling & Galvão 2022). To use the PROCODA code, we first need to fix a set of chemical reactions. In paper I, we consider 33 molecular species; among them, 5 were observed by IR techniques (4 irradiation products and acetonitrile) along with 240 chemical reactions (including dissociation, bimolecular, and termolecular rates) in addition to 33 individual desorption processes.

In paper I, we detailed the molecular column densities, chemical equilibrium stage, and effective reaction rates (Carvalho, Pilling & Galvão 2022). Here, we will focus on the desorption processes induced during ice irradiation. The experimental procedure was detailed before in several works such as Carvalho, Pilling & Galvão (2022), Pilling, Carvalho & Rocha (2022), Pilling et al. (2023a, c), and Pilling, da Silveira & Ojeda-Gonzalez (2023b). The desorption processes addressed here together with experimental studies and astronomical observations can help us to understand the gas-phase molecular abundances of acetonitrile in interstellar medium.

This work is organized as follows: in Section 2, we give more experimental and model details, in Section 3 we present the results, in Section 4 we discuss some astrophysical implications of this work, and finally in Section 5 we highlight our conclusions.

2 METHODOLOGY

2.1 Experimental data and the chemical reaction network

The experiment was performed in a high-vacuum chamber coupled to the spherical grating monochromator beamline at the facilities of the Brazilian Synchrotron Light Laboratory (LNLS). The beamline had a VUV + X-ray broad-band spectrum (from 6 eV up to 2 keV) in order to simulate the processing of acetonitrile ice by soft X-rays in astrophysical environments. The total irradiation time was around 1.5×10^4 s (final fluence of 1.5×10^{18} photons cm^{-2}); more experimental details can be found in Carvalho & Pilling (2020a).

To use the PROCODA code to study irradiation of acetonitrile ice analogues by X-rays, a chemical reaction network must be provided. In paper I, we gave the entire set of 240 chemical reactions that are considered (Carvalho, Pilling & Galvão 2022) and the effective reaction rates obtained. To build this reaction network, we analysed several studies on acetonitrile irradiation and its photoproducts (Hudson, Moore & Gerakines 2001; Hudson & Moore 2004; Hudson et al. 2008; Abdulgalil et al. 2013; McElroy et al. 2013; Carvalho & Pilling 2020a, 2022; Bulak et al. 2021). All such reactions were considered to happen between neutral species. The chemical reaction network had 33 molecular species and included 240 chemical reactions. Besides the 240 chemical reactions, a desorption reaction for each species was also considered.

2.2 Computational details

Column density data were available only for five species: CH_3CN, CH_3NC, H_2CCNH, CH_4, and HCN. Experimentally, the summed desorption yield has been determined to be 0.29 molecules per photon, so the desorption provides one of the constraints that are imposed in the code calculations. The code applies other constraints besides the desorption yield, namely minimization of χ^2 for the column density data, mass conservation, and chemical equilibrium stage. Those constraints are employed in a minimization process of a function, named score function (SF), that evaluates how close the system is to its minimum global solution. The SF is defined as follows:

$$\begin{aligned}
\mathrm{SF} = {} & p_1 \times \sum \frac{(\mathrm{oCH_3CN_{data}} - \mathrm{oCH_3CN_{model}})^2}{\mathrm{oCH_3CN_{data}}} \\
& + p_2 \times \sum \frac{(\mathrm{oCH_3NC_{data}} - \mathrm{oCH_3NC_{model}})^2}{\mathrm{oCH_3NC_{data}}} \\
& + p_3 \times \sum \frac{(\mathrm{oH_2CCNH_{data}} - \mathrm{oH_2CCNH_{model}})^2}{\mathrm{oCH_3CN_{data}}} \\
& + p_4 \times \sum \frac{(\mathrm{oHCN_{data}} - \mathrm{oHCN_{model}})^2}{\mathrm{oHCN_{data}}} \\
& + p_5 \times \sum \frac{(\mathrm{oCH_{4data}} - \mathrm{oCH_{4model}})^2}{\mathrm{oCH_{4data}}} \\
& + p_6 \times \left[(1 - \mathrm{MSC}_f) + (1 - \mathrm{MSCo}_f) + (1 - \mathrm{MSCo}_m)\right] \\
& + p_7 \times (1 - \mathrm{DSC}) + p_8 \times (1 - \mathrm{SSC}), \qquad (1)
\end{aligned}$$

where MSC_f is the model mass similarity criterion, and MSCo_f and MSCo_m are the column mass similarity criteria. The parameter DSC in equation (1) is the desorption similarity criterion, obtained by comparing the experimental desorption yield (Carvalho & Pilling 2020a) with the total molecular desorption yield computed by the model. Additionally, the parameter SSC is the slope similarity criterion. The first five terms in equation (1) define the summed χ^2 function for the data. The dimensionless parameters p_1 to p_8 employed in equation (1) are the weights of each term.

More details on the entire procedure can be found in Pilling et al. (2022, 2023a, c), including all steps of the code, such as input data management, assessment of initial conditions for rate constants, and search for a minimal global solution. It is worth to cite that a typical reaction in the chemical coupled system is written as

$$\begin{aligned}
\frac{\mathrm{d}N_i}{\mathrm{d}t} = {} & \left[-\mathrm{DES}_i(t) - \sum_{d1} k_{d1} N_i(t) - \sum_{d2} k_{d2} N_i(t) N_a(t)/L \right. \\
& \left. - \sum_{d3} k_{d3} N_i(t) N_a(t) N_b(t)/L^2 \right] \\
& + \left[\sum_{p1} k_{p1} N_i(t) + \sum_{p2} k_{p2} N_i(t) N_a(t)/L \right. \\
& \left. + \sum_{p3} k_{p3} N_i(t) N_a(t) N_b(t)/L^2 \right], \qquad (2)
\end{aligned}$$

where $\mathrm{d}N_i/\mathrm{d}t$ is the rate of change in the molecular column density of a given molecular species i, N_i is the molecular column density for the i species, and the k values are the reaction rates for dissociation, bimolecular, and termolecular processes (p indices stand for pro-

duction and *d* for destruction processes), and *L* indicates the sample average thickness in units of cm. The term DES_i is the column density desorbed to gas phase of the *i*th species, which is modelled in the following way:

$$DES_i = k_{DES,i}\Omega_i(t)N_i(t), \quad (3)$$

where $k_{DES,i}$ is called intrinsic desorption rate for the *i*th molecular species given in Hertz units and Ω_i is the dimensionless surface coverage of the *i*th species, defined as the column density of a given species over the sum of all column densities, $\Omega_i = N_i/\sum_i N_i$, and assumes values between 0 and 1. Behind equation (3) is a working hypothesis that the sample is uniform, so the desorption column density of a given species is proportional to the column density of the same species. The desorption reactions were considered to be first-order type ones. To determine the total column density of desorbed species, we simply summed all individual desorption column densities. We calculate the total desorption yield by using the total desorption column density, sample area, and radiation fluency.

3 RESULTS

In Fig. 1, we recall the best-fitting model obtained using the PROCODA code for the acetonitrile X-ray irradiation data. The figure shows the evolution of chemical concentrations for the 33 molecular species considered in the chemical reaction network. It is easy to see, particularly in panels (b) and (c), that at some points the curves cross each other, indicating that one species becomes more abundant than the other. This is important when analysing the desorption column densities (see equation 3).

In Fig. 2, the desorbed column densities for the 33 modelled species are presented. The desorbed column density of acetonitrile is at least two orders of magnitude larger than any other one. This indicates that the desorption processes are dominated by the acetonitrile molecule. However, from panel (a) of Fig. 1 it is also noticeable that acetonitrile concentration remains larger than the other ones during the entire irradiation procedure. This is understandable, once we have modelled the desorbed column densities as proportional to the concentrations (see also Fig. 1).

By comparing the CH and CH_3 concentrations, we can see that the difference in desorption rates can sometimes overcome the difference in concentrations, so a molecule with a smaller concentration can have a larger desorbed column density. The desorption rate for CH_3 is approximately 20 times larger than that for CH species. This difference in desorption rates is the main factor responsible for the higher desorbed column density for CH_3. So, it is noticeable that larger concentrations of a given species does not imply a larger desorption column density, this can also be perceived by comparing the results for H and CN species.

The H and CN concentration curves cross each other at around 6700 s after the beginning of the experiment, but desorption column density curves cross each other only at the instant 10 500 s, which represents a 3800 s delay. The desorbed column density of a given species depends on its concentration, desorption rate, and surface coverage (see equation 3). The surface coverage of a given molecular species is the ratio between its concentration to the sum of all molecular concentrations. So, if the desorbed column density of CN is higher than the H one, even when the concentration of H becomes higher, that can be addressed to the desorption rates. In fact, the intrinsic desorption rates for the species are presented in Table 1. From the table, one can note that the intrinsic desorption rates for H and CN species are slightly different, that is the reason why the desorption column density of H takes a certain time to overcome the CN one. It is also important to note that the H species takes a longer time to reach a steady state compared to the CN species, so the H species surpass the CN one in concentration and in desorption column density. If experimental data for H and CN were given, these results would be more conclusive.

The best-fitting model for the experimental data employing X-rays gives also a desorption yield, often called sputtering yield. This value was determined experimentally by employing an associative exponential equation to describe the evolution of molecular abundances of observed molecules (Carvalho & Pilling 2020b). With the help of mass conservation principle and assuming desorption column mass to be related only to the desorption of acetonitrile, $M_{DES} = MM_{CH_3CN}YF$, where MM_{CH_3CN} is the average molecular mass of acetonitrile, *Y* is the desorption yield, and *F* is the photon fluence, Carvalho & Pilling (2020b) obtained a total desorption yield around 0.29 molecule per photon. The value for desorption yield obtained within the best-fitting model was around 0.2 with an estimated ±20 per cent error, which is in good agreement with the experimental one.

Once the abundance of the father molecule acetonitrile is larger than the other ones, the acetonitrile desorbed column density dominates the total desorbed column density. One can observe that the desorbed column density of a given species is highly related to the concentration or abundance of that species. It is noticeable that the best-fitting model predicts H, CH, CN, and CH_2 as between the major photoproducts of acetonitrile irradiation, while from IR spectroscopy only HCN, CH_4, and acetonitrile isomers were identified. The H atom is not detectable from IR spectroscopy, whereas CH and CH_2 radicals have no reference spectra to be identified. However, the CN radical has an IR band close to 2085 cm^{-1}, which was used to identify HCN. The computational results presented here and the heating of acetonitrile sample (Carvalho & Pilling 2022), that revealed the appearance of more IR bands related to CN radical, indicates that 2085 cm^{-1} band is probably blended. This may introduce some error in our calculations.

In Fig. 3, the molecular desorption at chemical equilibrium for each species is given in panel a, whereas in panel b the intrinsic desorption rates are listed. The intrinsic desorption rates are determined by $k_{DES,i}$, given in equation (3). The larger intrinsic desorption rates are related to the species CH_3CN, H, CN, and CH_2. From panel (a) of Fig. 3, the molecular desorption at chemical equilibrium for acetonitrile represents almost 98 per cent of the total, and the other ones are much smaller with emphasis to H, CN and CH_2 species that virtually accounts for the other ∼2 per cent. In Table 2, we compare the desorption yields of this work with those presented by Basalgéte et al. (2023) for some species. In particular, the desorption yield for acetonitrile obtained here is almost three orders of magnitude higher; however, for HCN and CH_3 is between one and two orders smaller. The main difference between the experimental set-ups is the beam line. The authors of Basalgéte et al. (2023) used a 420 eV beam line, while in Carvalho & Pilling (2020b) authors used a broad-band beam line ranging from VUV to soft X-rays (6 eV to 2 keV) (see fig. 2 of Pilling & Bergantini 2015). The broad-band feature can be responsible for the higher desorption yield of acetonitrile because the large range of VUV photons can deposit more energy on the surface, thus increasing the photodesorption process. The large energy range can also have inner-shell resonance photons (C1s at 290 eV and N1s at 400 eV). Such resonance photons increase the interaction cross-sections with the radiation and also could allow greater desorption of acetonitrile molecules.

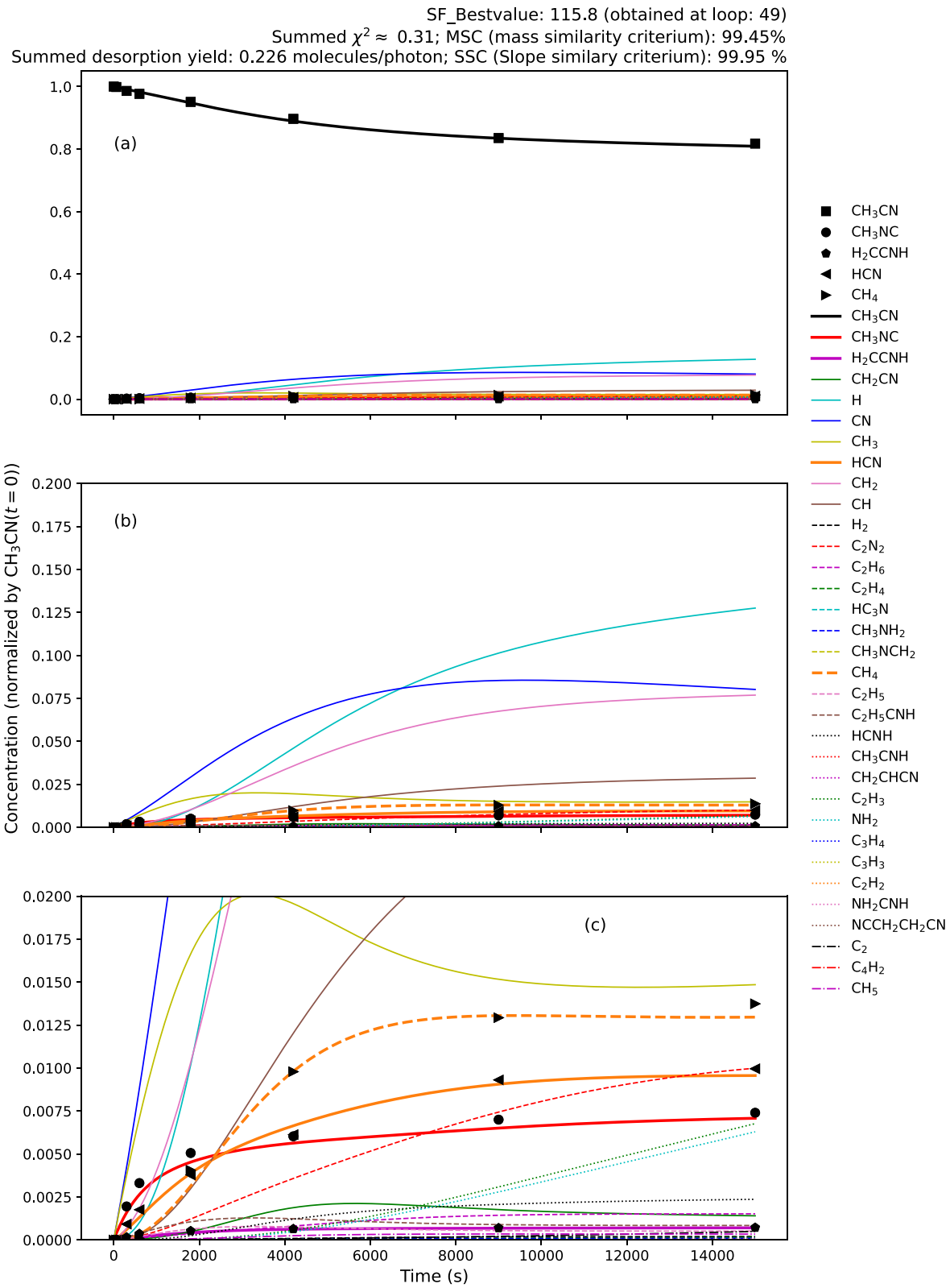

Figure 1. Concentration as a function of time. In panel (a), it is visible that the concentration of the father molecule is higher compared to the other species. Panels (b) and (c) highlight regions where concentration scales are smaller. Concentrations of all species are normalized by the initial concentration of CH_3CN.

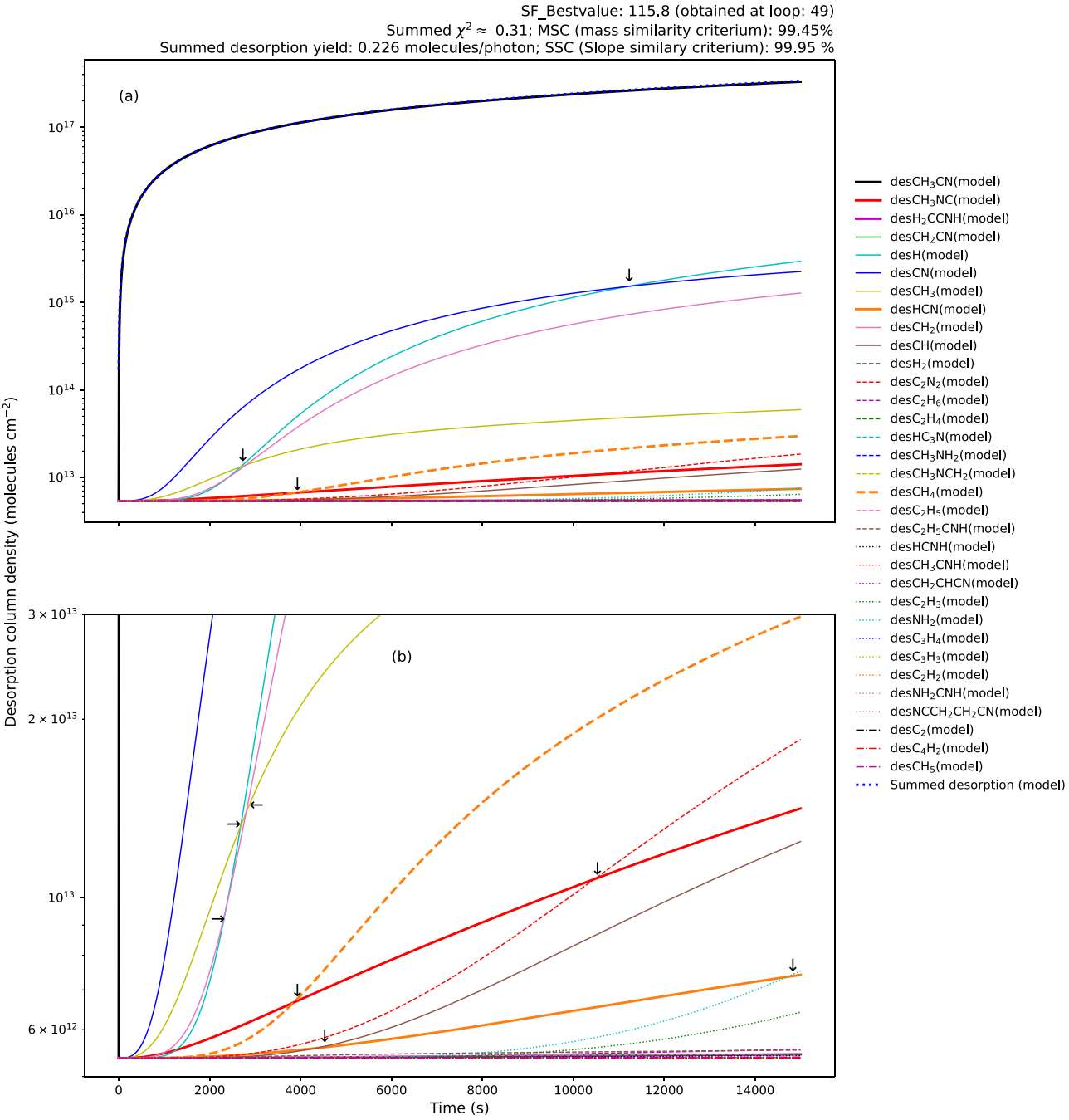

Figure 2. Panel (a): Molecular desorption induced by X-rays obtained by the best-fitting model in the mapping of chemical evolution of acetonitrile irradiated ice. Panel (b): Highlight of a region with smaller desorption column density values. In both panels, arrows indicate points where the desorption of a given species surpasses that of another one.

4 ASTROPHYSICAL IMPLICATIONS

We have seen that the amount of molecules desorbed to gas phase strongly depends not only on the concentration of that species, but also on the desorption rate and the time to reach chemical equilibrium. So, the desorption yield for each volatile species will depend on the radiation field, and the results presented here can be extrapolated to astrophysical environments, such as molecular clouds and protoplanetary discs. The results of Table 1 are also useful to improve astrochemical modelling that sometimes is based on gas-phase simulations instead of ice phase.

From Table 1, one can see that the largest intrinsic desorption rates are 6.2 $\times$ 10^{-6} s^{-1} (CH_3CN), 6.2 $\times$ 10^{-6} s^{-1} (CN), 5.7 $\times$ 10^{-6} s^{-1} (CH_2), 5.7 $\times$ 10^{-6} s^{-1} (H), 5.4 $\times$ 10^{-6} s^{-1} (C_3H_4), 5.1 $\times$ 10^{-6} s^{-1} (CH_3CNH), and 4.4 $\times$ 10^{-6} s^{-1} (C_2N_2). Hence, from the results of Fig. 2 and Table 1, it is expected that gas-phase observations of acetonitrile are related especially to the species H, CN, CH_2, and C_2N_2, so astrophysical observations could search for them. In fact, some of these molecules are often associated or concomitantly detected in astrophysical environments together with acetonitrile (see e.g. Woodney et al. 2002). The adenine nitrogenous base has been

Table 1. Intrinsic molecular desorption rates for each molecular species considered in the chemical reaction network.

Molecular species	Intrinsic desorption rate $k_{DES,i}$ (10^{-6} s^{-1})
CH_3CN	6.2
CH_3NC	3.5
H_2CCNH	2.9
CH_2CN	0.4
H	5.7
CN	6.2
CH_3	3.0
HCN	0.5
CH_2	5.7
CH	0.2
H_2	3.4
C_2N_2	4.4
C_2H_6	1.9
C_2H_4	1.6
HC_3N	2.2
CH_3NH_2	1.0
CH_3NCH_2	0.7
CH_4	2.9
C_2H_5	3.5
C_2H_5CNH	2.6
HCNH	0.3
CH_3CNH	5.1
CH_2CHCN	1.7
C_2H_3	1.4
NH_2	3.3
C_3H_4	5.4
C_3H_3	2.6
C_2H_2	0.9
NH_2CNH	0.8
$NCCH_2CH_2CN$	3.3
C_2	1.4
C_4H_2	2.6
CH_5	3.8

shown to survive solar X-ray fluxes during dozens of thousands of years (Pilling et al. 2011). Here, the photodesorption of X-ray irradiated acetonitrile ice leads to gas-phase H, CN, and C_2N_2, which can be combined to form adenine molecules via pentamerization processes (Roy, Najafian & von Ragué Schleyer 2007).

The photodesorption flux, Φ, of all molecular species after reaching chemical equilibrium can be estimated as

$$\Phi(F) = Y F, \tag{4}$$

where F represents photon fluence and Y represents the sputtering yield obtained by the best-fitting model ($Y = 0.2 \pm 0.04$ molecules per photon). Considering the photon flux, ϕ, to be constant, one obtains

$$\Phi(t) = Y \phi t, \tag{5}$$

where t represents time passed after chemical equilibrium. This gives an estimate of the time-scale for photodesorption processes to occur in astrophysical environments. The total desorption yield can be fragmented into each desorption yield for individual species; to do this, we multiply the total desorption yield, Y, by the desorption fraction of a given species, i.e. $DES_i/\sum_i DES_i$, so the desorption yield for that species will be given by the total desorption yield multiplied by its respective fraction. Finally, the photodesorption flux for a given species is calculated using equation (5) with its respective desorption yield.

Fig. 4 presents the photodesorption flux, individual and total, as a function of the photon flux. The coloured filled regions mark different domains of X-ray fluxes, related to the snow region of several objects, from compact to ordinary and young stars. The dotted vertical line marks the broad-band X-ray flux used during the ice irradiation experiment (Carvalho & Pilling 2020a). From the figure, one can see that the desorption flux induced by X-ray radiation field of white dwarfs at its snowline is of the order of 10^{-3} to 10^{0} molecules cm^{-2} s^{-1}, while the desorption flux for neutron star snowline is of the order of 10^{-1} to 10^{3} and black hole desorption flux is between 10^{3} and 10^{7}, and the photodesorption flux for the Sun and YSO objects is between 10^{6} and 10^{15} molecules cm^{-2} s^{-1}. In particular, at a distance of 9.5 au (Saturn orbit) the desorption flux is 1.6×10^{9} molecules cm^{-2} s^{-1}, which helps to understand desorption processes induced in Enceladus moon.

In Fig. 5 is presented the total column density desorbed as a function of time-scale after chemical equilibrium. Some fixed values for photon flux were considered, which are related to the X-ray flux astrophysical ices would be subjected to, e.g. the X-ray flux produced by the Sun at 1, 9.5 au (Saturn orbit), and 40 au (KBOs' typical orbit), and the X-ray flux of some compact objects at snowline distances. From the figure, it is noticeable that molecular desorption spans over a wide interval (10^{8}–10^{20} molecules cm^{-2}) for the 1 yr time-scale. At Saturn's orbit, the 1 yr time-scale corresponds to a total desorption of 10^{16} molecules cm^{-2}. These results are similar to those presented in Andrade, Rocco & Boechat-Roberty (2010), Almeida et al. (2014), and Pilling et al. (2019).

The Horsehead Nebula presented CH_3CN spectral lines that are 40 times brighter than those in the dense core, suggesting that thermal processes are not enough to explain these abundances (Gratier et al. 2013). The VUV photodesorption may explain the high gas-phase abundance of acetonitrile in the Horsehead Nebula, according to astrochemical modelling (Le Gal et al. 2017). The photodesorption yields obtained here are higher than those presented in Basalgéte et al. (2021, 2023) and contribute to the understanding that desorption explains the gas-phase abundances of acetonitrile in the Horsehead Nebula. The desorption rates obtained here can also be used to improve the previous results, while also helping to interpret gas-phase acetonitrile observations expected to be made by *JWST*.

5 CONCLUSIONS

From a previously used chemical reaction network for acetonitrile irradiated ice, we derive the column densities of observed and non-observed molecular species during the experiment and also the rate constants for the chemical reactions. Here, as a complement, we derive the desorbed column densities of observed and non-observed species and also give the desorption rates for each. These results can help to improve astrochemical modelling, and are relevant for analysing astrophysical scenarios, such as the surface of Saturn moon, Enceladus, which has nitrogen and oxygen compounds that are precursors of amino acids, the building blocks of life as we know.

The desorption process for a given species depends strongly on its concentration. In that case, after X-ray irradiation of a pure acetonitrile ice, the concentrations of all species are small compared to the acetonitrile one, so essentially the desorbed column densities of other species are also small. However, although acetonitrile dominates the total desorbed column density, the CN molecule has an intrinsic molecular desorption rate similar to the acetonitrile one. Other molecules with particular high intrinsic molecular desorption rates were H, H_2, CH_2, C_2N_2, CH_3CNH, and C_3H_4.

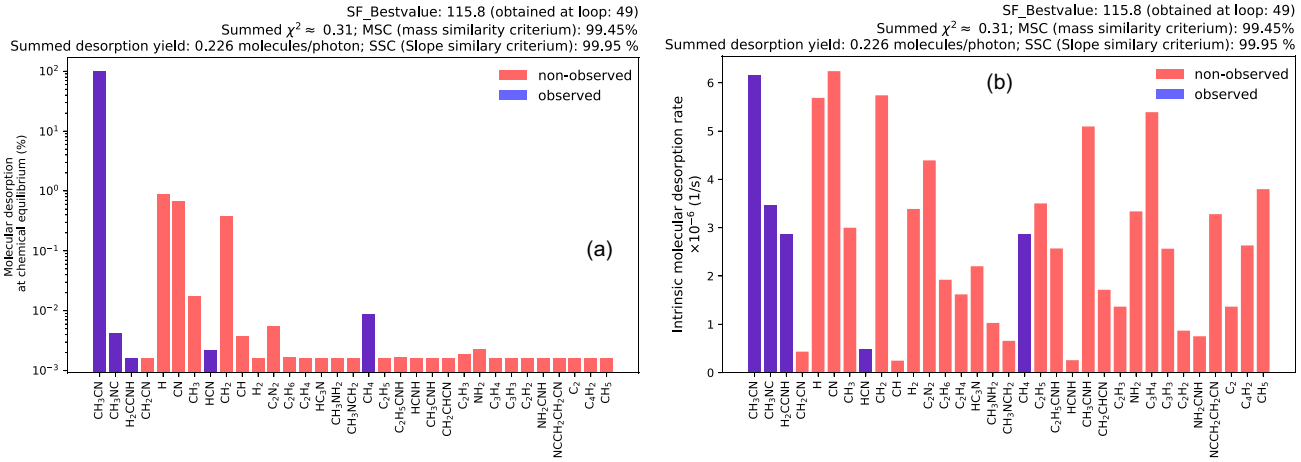

Figure 3. Panel (a): Molecular desorption of all molecular species at chemical equilibrium stage (or equilibrium branching ratio, EBR). Panel (b): Intrinsic molecular desorption rates at EBR.

Table 2. Desorption yields for the irradiation of pure acetonitrile ices with X-rays.

Molecular species	Desorption yield (molecules per photon)	X-ray beam line (eV)	References
CH_3CN	0.2 ± 0.04	6–2000	Carvalho & Pilling (2020a), this work
	$5.2 \pm 1.5 \times 10^{-4}$	420	Basalgéte et al. (2023)
HCN	$5.0 \pm 1.0 \times 10^{-6}$	6–2000	Carvalho & Pilling (2020a)
	$2.5 \pm 0.3 \times 10^{-3}$	420	Basalgéte et al. (2023)
CH_3	$4.0 \pm 0.8 \times 10^{-5}$	6–2000	Carvalho & Pilling (2020a)
	$1.3 \pm 0.7 \times 10^{-3}$	420	Basalgéte et al. (2023)

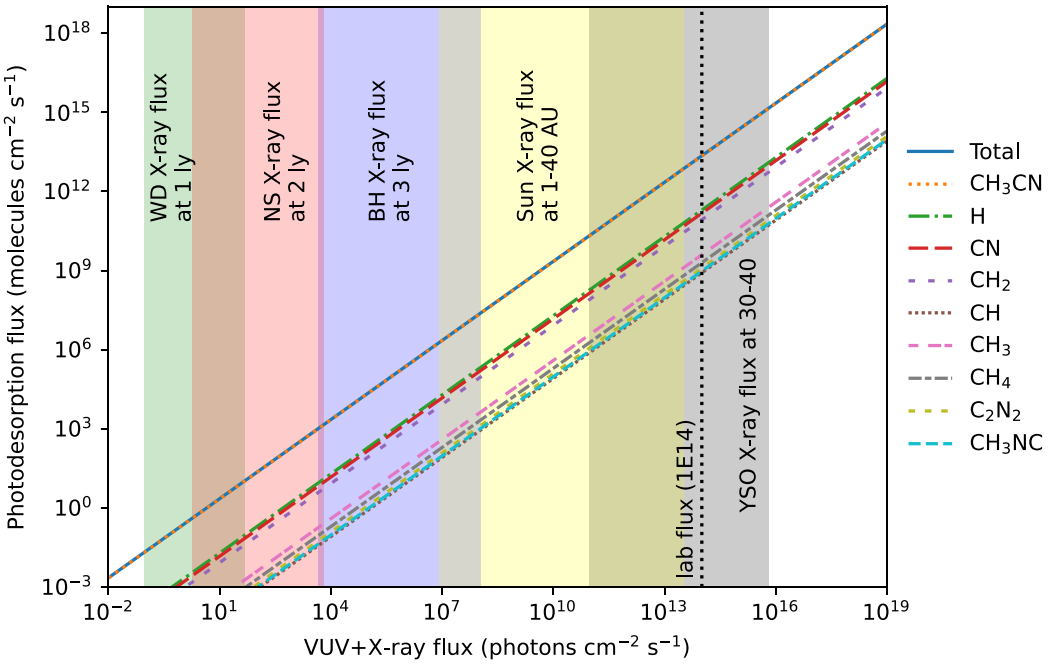

Figure 4. Desorption flux as a function of photon flux in the range of 6 eV to 2 keV for selected molecular species with higher abundances at chemical equilibrium and high desorption rates. The vertical dotted line marks the broad-band X-ray flux of 10^{14} photons cm^{-2} s^{-1}, which corresponds to laboratory photon flux used during the ice irradiation experiment. The colour filled regions correspond to typical white dwarf X-ray fluxes at 1 ly distances (green), typical neutron star X-ray fluxes at 2 ly distances (red), typical black hole X-ray fluxes at 3 ly distances (blue), Sun's X-ray fluxes from 1 to 40 au (yellow), and YSO models of X-ray flux at ∼30–40 au (grey) (see the text for more details).

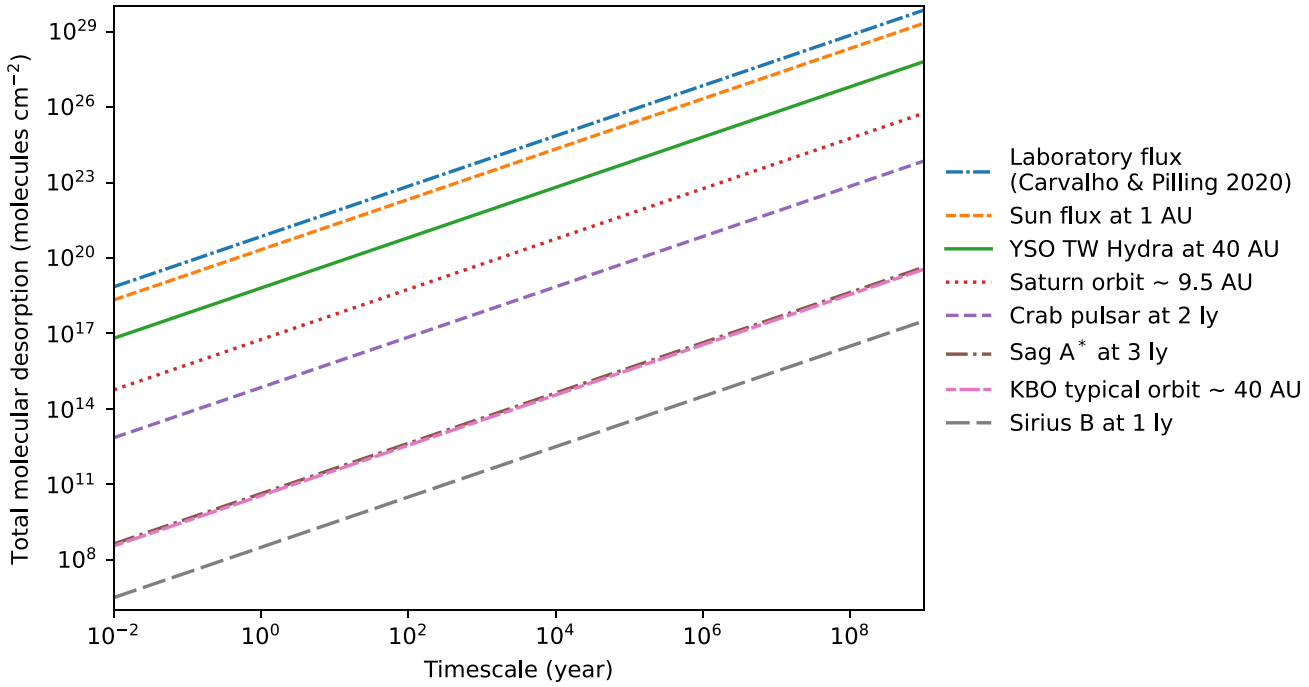

Figure 5. Total molecular desorption induced on acetonitrile-rich ices by broad-band X-ray bombardment as a function of time-scale after reaching chemical equilibrium (see equation 3). Each curve corresponds to a given fixed photon flux related to several astrophysical objects.

The higher values of intrinsic desorption rates of CN and C_2N_2 help to explain the IR absorbance band of 4.8 μm as HCN. At experimental chemical equilibrium, the acetonitrile molecular desorption is still much larger than any other one. Except for acetonitrile, the molecules with higher molecular desorption at chemical equilibrium are H, CN, and CH_3.

The desorption flux and the time-scales of molecular desorption were derived for several astrophysical environments, such as the Saturn's orbit, where the desorption flux will be between 10^6 and 10^9 molecules cm^{-2} s^{-1} and the molecular desorption for a 1 yr time-scale is around 10^{16}, results that are relevant for Enceladus. The results obtained here help also to explain the gas-phase abundance of acetonitrile in the Horsehead Nebula.

ACKNOWLEDGEMENTS

The authors acknowledge the financial support of Fundação Araucária under the project Novo Arranjo de Pesquisa e Inovação-NAPI 'Fenômenos Extremos no Universo'. The authors also acknowledge the Brazilian research agencies Conselho Nacional de Desenvolvimento Científico e Tecnológico – CNPq (#306145/2015-4, #302985/2018-2) and Coordenação de Aperfeiçoamento de Pessoal de Nível Superior – CAPES (#PNPD/88887.368365/2019-00, #PNPD/88887.751149/2022-00). SG acknowledges Fundação Araucária for financial support.

DATA AVAILABILITY

The data that support the findings of this study are available from the corresponding author upon reasonable request.

REFERENCES

Abdulgalil A. G. M. et al., 2013, Phil. Trans. R. Soc. A, 371, 20110586
Almeida G. C., Pilling S., Andrade D. P. P., Castro N. L. S., Mendoza E., Boechat-Roberty H. M., Rocco M. L. M., 2014, J. Phys. Chem. C, 118, 6193
Andrade D. P. P., Rocco M. L. M., Boechat-Roberty H. M., 2010, MNRAS, 409, 1289
Andron I., Gratier P., Majumdar L., Vidal T. H. G., Coutens A., Loison J.-C., Wakelam V., 2018, MNRAS, 481, 5651
Basalgéte R., Ocaña A. J., Féraud G., Romanzin C., Philippe L., Michaut X., Fillion J.-H., Bertin M., 2021, ApJ, 922, 213
Basalgéte R. et al., 2023, A&A, 676, A13
Beltrán M. T., Cesaroni R., Codella C., Testi L., Furuya R. S., Olmi L., 2006, Nature, 443, 427
Bergner J. B., Guzmán V. G., Öberg K. I., Loomis R. A., Pegues J., 2018, ApJ, 857, 69
Bøgelund E. G., McGuire B. A., Hogerheijde M. R., van Dishoeck E. F., Ligterink N. F. W., 2019, A&A, 624, A82
Bulak M., Paardekooper D. M., Fedoseev G., Linnartz H., 2021, A&A, 647, A82
Carvalho G. A., Pilling S., 2020a, J. Phys. Chem. A, 124, 8574
Carvalho G. A., Pilling S., 2020b, MNRAS, 498, 689
Carvalho G. A., Pilling S., 2022, Spectrochim. Acta A, 267, 120495
Carvalho G. A., Pilling S., Galvão B. R. L., 2022, MNRAS, 515, 3760
Corazzi M. A., Brucato J. R., Poggiali G., Podio L., Fedele D., Codella C., 2021, ApJ, 913, 128
Crovisier J., 1998, Faraday Discuss., 109, 437
Gerakines P. A., Moore M. H., Hudson R. L., 2004, Icarus, 170, 202
Goesmann F. et al., 2015, Science, 349, aab0689
Gratier P., Pety J., Guzmán V., Gerin M., Goicoechea J. R., Roueff E., Faure A., 2013, A&A, 557, A101
Hudson R. L., Moore M. H., 2004, Icarus, 172, 466
Hudson R. L., Moore M. H., 2006, Astrobiology, 6, 483
Hudson R. L., Moore M. H., Gerakines P. A., 2001, ApJ, 550, 1140
Hudson R. L., Moore M. H., Dworkin J. P., Martin M. P., Pozun Z. D., 2008, Astrobiology, 8, 771

Huebner W. F., Snyder L. E., Buhl D., 1974, Icarus, 23, 580
Iino T., Sagawa H., Tsukagoshi T., 2020, ApJ, 890, 95
Kanda K., Nagata T., Ibuki T., 1999, Chem. Phys., 243, 89
Lara L. M., Lellouch E., López-Moreno J. J., Rodrigo R., 1996, J. Geophys. Res. Planets, 101, 23261
Le Gal R., Herbst E., Dufour G., Gratier P., Ruaud M., Vidal T. H. G., Wakelam V., 2017, A&A, 605, A88
Le Gal R., Brady M. T., Öberg K. I., Roueff E., Le Petit F., 2019, ApJ, 886, 86
Lee J.-E. et al., 2019, Nat. Astron., 3, 314
Loomis R. A., Cleeves L. I., Öberg K. I., Aikawa Y., Bergner J., Furuya K., Guzman V. V., Walsh C., 2018, ApJ, 859, 131
McElroy D., Walsh C., Markwick A. J., Cordiner M. A., Smith K., Millar T. J., 2013, A&A, 550, A36
Marten A., Hidayat T., Biraud Y., Moreno R., 2002, Icarus, 158, 532
Moore M. H., Khanna R., Donn B., 1991, J. Geophys. Res. Planets, 96, 17541
Moore M. H., Ferrante R. F., Nuth J. A., 1996, Planet. Space Sci., 44, 927
Öberg K. I., Guzmán V. V., Furuya K., Qi C., Aikawa Y., Andrews S. M., Loomis R., Wilner D. J., 2015, Nature, 520, 198
Öberg K. I. et al., 2021, ApJS, 257, 1
Pilling S., Bergantini A., 2015, ApJ, 811, 151
Pilling S., Duarte E. S., Domaracka A., Rothard H., Boduch P., da Silveira E. F., 2010, A&A, 523, A77
Pilling S. et al., 2011, MNRAS, 411, 2214
Pilling S., Rocha W. R. M., Freitas F. M., da Silva P. A., 2019, RSC Adv., 9, 28823
Pilling S., Carvalho G. A., Rocha W. R. M., 2022, ApJ, 925, 147
Pilling S., Rocha W. R. M., Carvalho G. A., de Abreu H. A., 2023a, Adv. Space Res., 71, 5466
Pilling S., da Silveira C. H., Ojeda-Gonzalez A., 2023b, MNRAS, 523, 2858
Pilling S., Carvalho G. A., de Abreu H. A., Galvão B. R. L., da Silveira C. H., Mateus M. S., 2023c, ApJ, 952, 17
Roy D., Najafian K., von Ragué Schleyer P., 2007, Proc. Natl. Acad. Sci. USA, 104, 17272
Snyder L. E., Buhl D., 1971, ApJ, 163, L47
Solomon P. M., Jefferts K. B., Penzias A. A., Wilson R. W., 1971, ApJ, 168, L107
Taniguchi K., Guzmán A. E., Majumdar L., Saito M., Tokuda K., 2020, ApJ, 898, 54
Thelen A. E. et al., 2019, Icarus, 319, 417
Thelen A. E. et al., 2020, ApJ, 903, L22
Vasconcelos F. de A., Pilling S., Rocha W. R. M., Rothard H., Boduch P., 2017, ApJ, 850, 174
Willis E. R., Garrod R. T., Belloche A., Müller H. S. P., Barger C. J., Bonfand M., Menten K. M., 2020, A&A, 636, A29
Woodney L. M. et al., 2002, Icarus, 157, 193

This paper has been typeset from a TEX/LATEX file prepared by the author.